Pressure transient and vaporization process following the rapid heating of a liquid - Experiments and modelling

Jean Muller, Romuald Rullière, Pierre Ruyer, Marc Clausse

Graphical Abstract

Pressure transient and vaporization process following the rapid heating of a liquid - Experiments and modelling

Jean Muller, Romuald Rullière, Pierre Ruyer, Marc Clausse

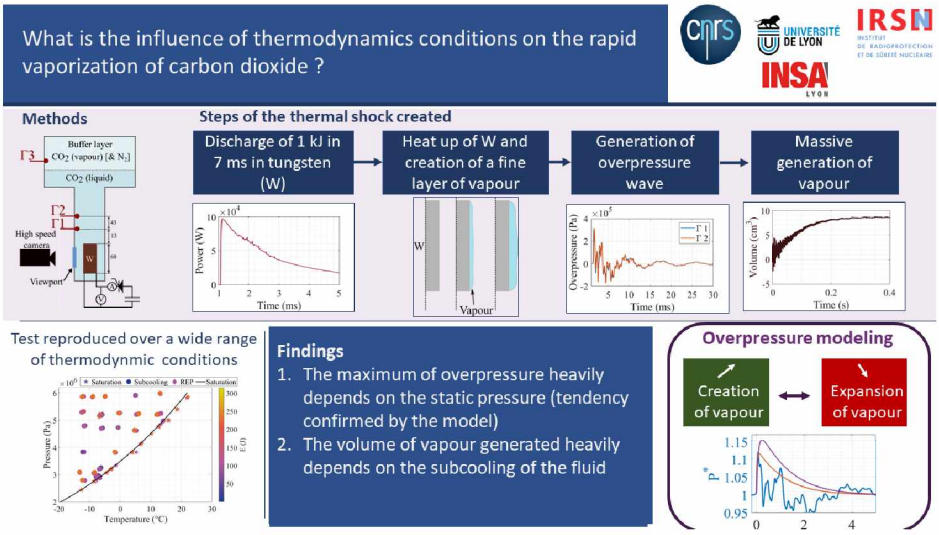

Highlights

Pressure transient and vaporization process following the rapid heating of a liquid - Experiments and modelling

Jean Muller, Romuald Rullière, Pierre Ruyer, Marc Clausse

- Thermal shock implies the rapid creation of a layer of vapour
- The increase of pressure depends on the dynamics of creation of vapour
- The violence of the phenomena decreases with the pressure and the sub-cooling
- Peak pressure observed at onset of vapour formation is related to expansion dynamics of a vapour layer

Pressure transient and vaporization process following the rapid heating of a liquid - Experiments and modelling

Jean Muller[a,b], Romuald Rullière[b], Pierre Ruyer[a], Marc Clausse[b]

[a] *Institut de Radioprotection et de Sûreté Nucléaire (IRSN), PSN-RES/SEMIA/LSMA, BP3, St Paul-Lez-Durance 13115, France*
[b] *Univ. Lyon, CNRS, INSA Lyon, CETHIL, UMR5008, Villeurbanne, F-69621, France, Université Lyon 1, F-69622, France*

Abstract

The aim of this paper is to study the influence of the thermodynamic conditions on the consequences of the rapid vaporization of CO_2. This study is motivated by the lack of experiments characterizing those transient phenomena over a wide range of thermodynamic conditions. For that purpose, a complete test section was designed based on the Joule effect to deliver the energy discharge in pressurized CO_2.

The transient deposit of power in the liquid have two consequences: the generation of a pressure wave (of several bars) due to the transient creation of vapour, and a slow compression in the test section due to the creation and expansion of vapour (few cm^3). This experiment had been performed 200 times over a wide range of thermodynamic conditions: static pressure between 2.55 MPa and 6 MPa, liquid temperature between -12 °C and 22 °C and energy transmitted to the fluid between 70 J and 310 J. From this databank, significant tendencies are extracted from the maximum of overpressure generated and the mass of vapour created function of the test conditions. Lastly, a simple model permits to predict the first pressure peak as a function of the test conditions.

This work, motivated by the so-called Fuel Coolant Interaction (FCI) nuclear safety related problematic, brings consistent data allowing to better characterize the small scale processes for such transient vaporization phenomena.

Keywords: Boiling, Pressure peak, Experiment, Phase Change, Joule effect

Postprint for Experimental Thermal and Fluid Science

Nomenclature

Exponent

$*$	Non dimensionnal

Greek symbols

ϵ	Calculation error(%)
Γ	Overpressure (Pa)
γ	Modified Laplace's coefficient
ω	Mass fraction
ρ	Density (kg.m^{-3})
τ_{sf}	Time scale of creation of vapour (s)
Θ	Number theta ($\Theta = (E/(c_{pl}(T_i - T_{sat})P_i) + \mathcal{L})/m_f$)

Latin symbols

$\dot{m}_0$	Initial mass flow rate of vapour (kg.s^{-1})
$\mathcal{L}$	Specific latent heat of CO_2 (J.kg^{-1})
c	Sound velocity (m.s^{-1})
c_{P_i}	Specific heat capacity (J.kg^{-1}.K^{-1})
E	Energy (J)
I	Current (A)
Ja	Jakob number ($Ja = (\rho_l/\rho_v)(c_{pl}(T_i - T_{sat})P_i)/\mathcal{L}$)
M	Molar mass (44×10^{-3} kg.mol^{-1} for CO_2 and 14×10^{-3} kg.mol^{-1} for N_2)
m	Mass (kg)
N_0	Model's parameter ($N_0 = m_{v,max}/(\dot{m}_0\tau_{sf})$)
N_1	Model's parameter ($N_1 = (\rho_v/\rho_l)(P_i/c)(S/\dot{m}_0)$)

P_c Critical pressure of carbon dioxide (7.27×10^6 Pa)

P_i Initial static pressure (Pa)

P_r Reduced pressure ($P_r = P_i/P_c$)

R Gas constant

S Surface (m^2)

T Temperature (K)

t Time (s)

U Voltage (V)

u Velocity ($m.s^{-1}$)

V Volume (m^3)

z Vapour compressibility factor of carbon dioxide

Subscript

f Fluid

i Initial

l Liquid

m Maximum

sat Saturation

v Vapour

1. Introduction

During Reactivity Initiated Accident (**RIA**) scenario in nuclear power plants, some fuel rods are submitted to a huge power peak and may endure high mechanical and thermal stresses. This accident has been studied in different reactors presented in [1]. In the Nuclear Safety Research Reactor (**NSRR**), situated in Japan, more than 400 RIA tests were performed. Each test consists in depositing a defined amount of energy in a piece of a nuclear rod, to reproduce the power transient observed during a RIA. The results of these tests are summarized in [2] and show consistent degradation for an energy deposited superior to $800\,\mathrm{kJ.g}_{UO_2}^{-1}$. The clad failure consequences following an RIA have not to be considered for the safety demonstration of typical PWR fuel rods, [3], but is still a matter of interest for some seldom cases, [4]. IRSN drives research programs on this topic, e.g. [5] and this study is a focus on the more specific fuel-coolant thermal interaction.

Let us therefore consider, in this paper, the case of a failure of the nuclear rod. Subsequently, the fuel contained in the rod is ejected toward water coolant. Past experiments realized in NSRR reproduces such failure consequences and are presented in [6] (TK-2 and JMH-5 tests). In both tests, a portion of a pre-irradiated fuel rod undergoes a pulse irradiation before failure. The main consequence of the failure is the ejection of a mass of fuel and gas into the coolant (water at atmospheric pressure and ambient temperature). The instantaneous contact between hot particles (around 2000 K) and cold fluid (293.15 K) creates a thermal shock. The tests then show phenomena of different time scales and intensities: a high intensity with a small time scale compression (2 MPa in less than 1 ms) and a smaller compression with longer time scale (22 to 68 J of mechanical work generated in 30 ms).

The generation of a pressure wave of 2 MPa could be explained by the transient creation of a layer of vapour on the heated surfaces. The study of pressure transients due to the rapid creation of vapour is not extensively performed in the literature. Only two works achieved at small scales are relevant. These work were delivered by [7] and [8] which use micrometric heated surfaces (rectangle of $100\,\mu m \times 110\,\mu m$ for [7] and Pt wire of $10\,\mu m$ in diameter for [8]). In [7], the authors correlate the acceleration of volume of vapour created (d^2V/dt^2) with the rate of increase of pressure (dP/dt) which is equal to $10\,\mathrm{GPa.s}^{-1}$ for a deposit of $62\,\mu\mathrm{J}$ in $6\,\mu\mathrm{s}$ (resulting in a power per unit of surface of $1\,\mathrm{GW.m}^{-2}$). In [8], the measured overpressure (from 1 to 10 bar) is proportional to the power deposited (from 7 to 42.5 W), as

expected.

The works performed by [7] and [8] finely detail the phenomena occurring in water at atmospheric pressure and ambient temperature but do not study the phenomena for other thermodynamic conditions. The present work has three main aims:

- To finely characterize the phenomena under saturation conditions. This is done to describe each step of the thermal shock, as performed in [7].
- To reproduce the same thermal shock over a wide range of thermodynamic conditions and then providing a database of tests (that does not exist in the literature).
- To study the influence of the thermodynamic conditions on the phenomena.

In order to accomplish these tasks, an experiment was mounted (see, [9] and [10]) and named EDITE (**E**tude d'un **D**épôt **I**mportant et **T**ransitoire d'**E**nergie). This experimental device allows for rapid thermal energy transfer toward a pressurized vessel of liquid CO_2. The CO_2 had been chosen because it could be used in thermodynamic similarity with the water under nuclear reactor conditions at lower pressure and temperature (and then lower costs and maintenance), i.e. the reduced pressure and the thermodynamic qualities are equal between the water at (P_i, T_i)=(15.5 MPa, 305 °C) and the CO_2 at (P_i, T_i)=(5.2 MPa, -6 °C) [See [10]].

With this experiment, more than 200 tests have been performed over a wide range of thermodynamic conditions (from nuclear conditions that corresponds to an initially subcooled liquid CO_2 to liquid at saturation) to study the influence of the test conditions on the phenomena described in section 2. The obtained database permits extracting significant tendencies for the maximum overpressure and the volume of vapour created, presented in the section 3. Finally, a model of the pressure generation during the first instants of the creation of vapour shows tendencies that are interpreted in the section 4 of this paper.

2. Methods and Results Overview

2.1. Test section

The test section is presented in figure 1a. The heating element is inserted in a test section filled with pressurized carbon dioxide and composed of a

wide tank (200 mm in diameter) placed on the top of a long and narrow tube (31 mm in diameter). It consists in three fine plates of tungsten (W in figure 1a) assembled to each other with brass screws and presented in figure 1b. Each tungsten plate is 60 mm high, 21 mm wide and 0.4 mm thick.

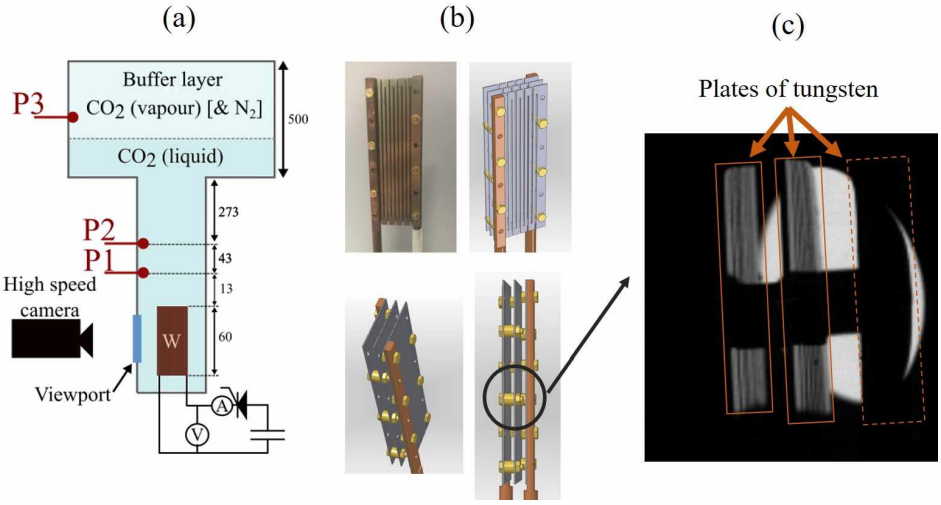

Figure 1: Experimental setup (a), the heating element composed of tungsten sheets (b) and the raw frame recorded by the camera (c)

Heat is produced by Joule effect thanks to the discharge of 9 capacitors, of 3 mF each, into the heating element. A static pressure sensor and a PT100 record the test conditions before and after the capacitor discharge. The electrical power deposited in the heating element is measured by a voltage sensor and a current sensor recording at 500 kHz. Three dynamic pressure sensors used at 500 kHz are placed along the tube ($\Gamma 1$ and $\Gamma 2$) and in the buffer layer ($\Gamma 3$) to record the pressure transients. The acquisition of these quantities was done by a National Instrument's system composed of compact DAQ 9188, two NI 9223 ($\pm 10\,V$ for the overpressure and power measurement) and a NI 9203 ($4 - 20$ mA for static pressure, temperature and liquid level measurements). The detailed acquisition system is presented in [11].

A high-speed camera allows for observing two surfaces of the heating element as shown in the figure 1c (Plates of tungsten- plain orange blocks). The third plate of tungsten (dotted orange block) is hidden by the copper bar. The sampling rate is equal to 15 kHz, for a resolution of $9.2\,\mathrm{px.mm^{-1}}$.

At the top of the test section, a buffer layer is used to regulate the static

pressure. It is composed of vapour of carbon dioxide and gaseous nitrogen (optional). The nitrogen is added in the test section to increase the pressure and to perform tests at sub-cooled conditions. The temperature is controlled by a climatic chamber that enclosed the test section.

2.2. Overpressure transient

A test has been performed at (P_i, T_i, E)=(2.55 MPa, -12.5 °C, 232 J). The electrical power deposited in the heating element is plotted in the figure 2a. It exhibits an instantaneous increase to 10^5 W, and a slow decrease to zero in 5 ms. The total energy (232 J) is deposited in the tungsten in less than 5 ms.

Due to the transient deposit of power, the tungsten is heated up to 77 °C in 4 ms ($dT/dt = 19\times10^3$ K.s^{-1}). During the power deposit, the overpressure is recorded a few millimetres away from the tungsten($\Gamma1$ & $\Gamma2$) and in the buffer layer ($\Gamma3$). $\Gamma1$ and $\Gamma2$ are plotted in figure 2b and exhibit the same trend: a first increase to a maximum of 3×10^5 Pa, then an oscillating decrease which reaches zero for $t > 25$ ms. The oscillating decrease is due to acoustic rebounds of the pressure wave inside the test section (due to abrupt modification of diameter and solid walls), see [10]. During the first increase of pressure, both overpressure ($\Gamma1$ and $\Gamma2$) are delayed by a constant time equals to 0.066 ms and they exhibit the same increase rate to the first peak, which is equal to 1.5 GPa.s^{-1}. Following their maximum, both overpressures are no longer simply delayed because of acoustic rebounds of the pressure wave ("Acoustic behaviour" on figure 2b).

Four snapshots of the heating element with an adjusted contrast are presented on figure 2c. They are taken at 1, 1.47, 1.6 and 2.53 ms, respectively. Each snapshot, except the one taken at 1 ms, is spotted on the overpressure plot thanks to a vertical dark dot line. The first snapshot is taken before the start of the power deposit at $t = 1$ ms. Two surfaces of the heated element are distinguishable, with light gray colour. At the start of the power deposit, the tungsten is heated up and the surfaces become darker at $t = 1.47$ ms (second snapshot). The dark regions on the surfaces of tungsten grow with time revealing that it embodies a small layer of vapour created during the deposit of power. At the same instant, the overpressure starts to increase. Then on the third snapshot, both visible surfaces are covered with a layer of vapour. At the same instant, the overpressure reaches its maximum. The fine layer grows over time and at $t = 2.53$ ms small bubbles are distinguishable over

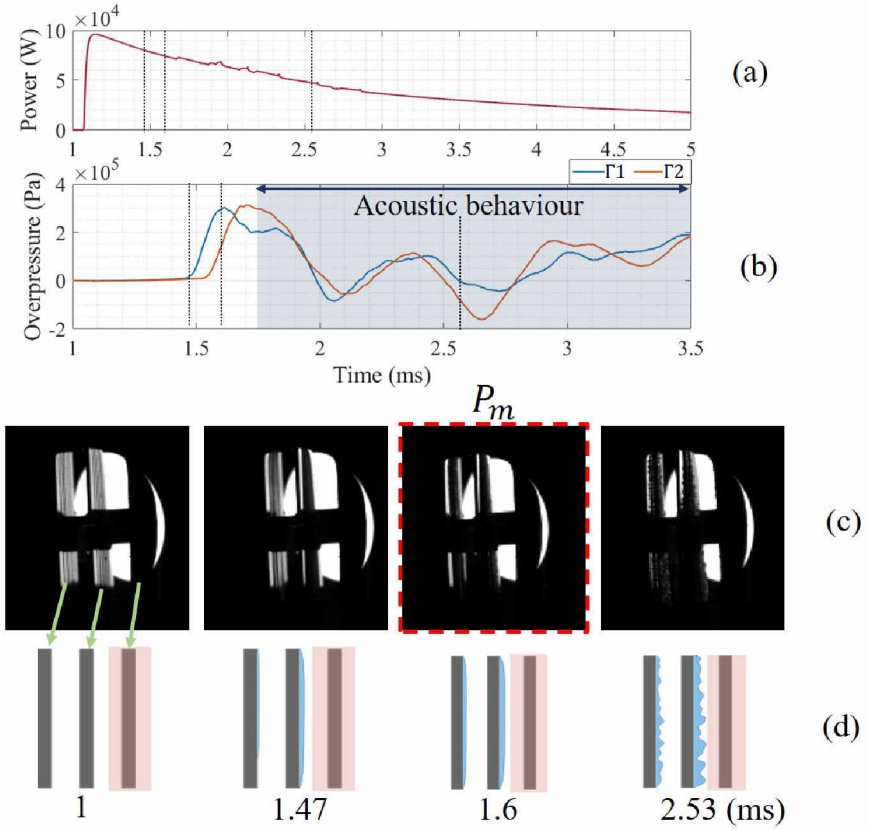

Figure 2: Overview of the first stages of the thermal shock: electrical power (a), overpressure Γ1 and Γ2 (b), selected snapshot of the heating element (c) with adjusted contrast and the sketch of the creation of vapour (d).

the tungsten sheets. Due to the low resolution of the snapshots, a sketch of a side view of the boiling process is presented on figure 2d. It represents the steps observed on figure 2c. On the visible sheets of tungsten (grey boxes) a small layer of vapour (blue) is created, grows over time and forms a bubbly surface (2.53 ms). The third plate of tungsten is shadowed in red because it could not be observed in these snapshots. Therefore it is assumed that the vapour quickly forms a layer over the plate as it can be revealed by the high speed camera. This kinetics of vapour formation is observed on the 200 tests performed and presented in the section 3.

Visual observation in the experiment does not allow any identification of the nucleation site density, the process of vapour formation appears to

be rather homogeneous over the plates. This can be related to literature results concerning the nucleation process for such rapid wall heating transients. In [12], the authors reported their analysis of very various experiments in such conditions and show that the process deviates from the scaling with nucleation site density (NSD), reaching a so-called Heterogeneous Spontaneous Nucleation regime. It is described in [13] that reported increase of the NSD with heating rate till a plateau behavior for which a bubble generation regime "in which a large number of tiny bubbles with almost uniform diameter generated concurrently on the heater" is observed. This corresponds to the actual case of our experiments.

The correlation between the transient creation of a layer of vapour on the tungsten sheets and the increase of overpressure measured few millimeters from the tungsten proves that the overpressure is due to transient creation of vapour. This phenomenon is equivalent to the one observed by [7] for micrometric heaters. However, the rate of increase of pressure is one order of magnitude higher in the cited paper ($10\,\mathrm{GPa.s^{-1}}$ for [7] and $1.5\,\mathrm{GPa.s^{-1}}$ for this work). This difference is mainly due to the difference in heating rate ($50\times10^6\,\mathrm{K.s^{-1}}$ for [7] and $0.02\times10^6\,\mathrm{K.s^{-1}}$ for the present work) and to the difference of thermodynamic condition (high subcooling in water for the work of [7] and saturation conditions for the present work).

2.3. Mass of created vapour

Following the described transient of pressure seen on the figure 2, the layer of vapour grows over time and reaches a maximum of volume which obstructs the viewport. The massive creation of vapour at the bottom of the test section moves the liquid column which compresses the buffer layer. The figure 3 summarizes this dynamic in three main steps:

1. Before the power deposit, the test section is composed of a column of liquid and a buffer layer of volume V_i at the top of it.

2. During the power deposit, a volume of vapour V_v is created at the bottom of the test section. The creation of vapour pushes the liquid column which compresses the buffer layer of a volume $V_i - V(t)$.

3. A maximum of volume of vapour is reached.

The compression of the buffer layer is measured by the dynamic pressure sensor $\Gamma 3$ (see figure 1a) and exhibits a maximum of compression correspond-

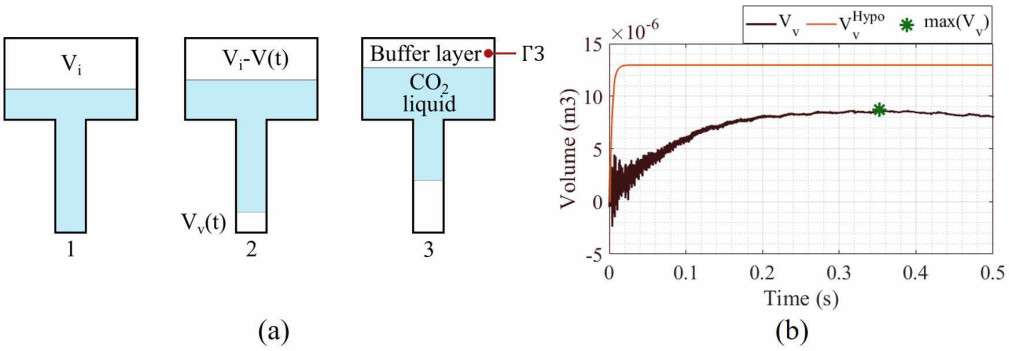

Figure 3: (a)-Compression of the test section due to the creation of vapour. (b)-Volume of vapour created over time V_V and compared to the theoretical volume V_V^{Hypo}.

ing therefore to the maximum of volume of vapour generated. Under the assumption of isentropic compression of the buffer layer, the volume of vapour created during the test is calculated with the equation (1). The large amount of vapour in the buffer (11.6 L) and the small time scale (under 1 s) of the compression justify the use of an isentropic assumption for the calculation.

$$V_v(t) = V_i \left(1 - \left(\frac{P_i}{P_i + \Gamma_3(t)}\right)^{1/\gamma}\right) \frac{1}{1 - \rho_v/\rho_l} \tag{1}$$

With ρ_v and ρ_l the density of the vapour and of the liquid, respectively. The number γ is expressed as follows,

$$\gamma = \frac{c_{P_i}^{(v)}}{c_{P_i}^{(v)} + K} \quad \text{with} \quad \begin{cases} c_{P_i}^{(v)} = \omega_{CO_2} c_{P_i,CO_2}^{(v)} + (1 - \omega_{CO_2}) c_{P_i,N_2}^{(v)} \\ K = \omega_{CO_2} \frac{zR}{M_{CO_2}} + (1 - \omega_{CO_2}) \frac{R}{M_{N_2}} \end{cases} \tag{2}$$

The volume of vapour calculated thanks to the equation (1) is plotted in figure 3b. This calculated volume (V_v) increases in 0.35 s to a maximum equal to 9 cm^3. In the same figure, the volume of saturated vapour that could be generated from the instantaneous amount of energy deposited in the tungsten, named V_v^{Hypo}, is plotted. The calculated volume grows from zero to a maximum equal to 13 cm^3 with the time scale of the capacitors discharge (5 ms) and then keeps the maximum value (no recondensation assumption). It shows that the volume of generated vapour is close to this theoretical value: most of the deposited energy leads to mass transfer from liquid to vapour. The

vaporization process is slower than the energy deposit in the tungsten due to the storage of specific energy within the tungsten. The difference of kinetics is then due to the fact that heat and mass transfers at the tungsten wall are the limiting processes for this vaporization.

The discrepancy between the maximum of both volumes, presented on figure 3b, is discussed for all the tests in the next section. This matter is still under investigation for future tests but it could be explained by the recondensation of the vapour. Even at saturated conditions, the recondensation of the vapour could be observed [14] and generates a gap between the maximum of volume of vapour calculated from the maximum of compression of the buffer layer (maximum of Γ_3) and the volume of vapour corresponding to the heat released in the liquid CO_2 (theoretical).

3. Experimental Results and Discussion

In order to study the influence of the thermodynamic conditions on the consequences of the thermal shock, 200 tests were performed over a wide range of pressure, temperature and energy. For all the tests performed, the same qualitative behaviour, described in the previous section, is observed. Namely, for each condition, the value of the first overpressure peak, denoted Γ_m, is measured by Γ1. The maximum of volume of vapour, V_v, is deduced from Γ3. The influence of the thermodynamic conditions on these parameters is studied in this section.

To facilitate the read, the points used to seek tendencies on the figures presented in this section are of the same size than the uncertainties of the measured values (see Appendix A).

3.1. Thermodynamics conditions

The test conditions are presented in figure 4a. This figure shows all the tests in a (P_i, T_i) diagram, with P_i the static pressure and T_i the temperature of the fluid at the instant of the power deposit. The colour scale represents the energy deposited in the tungsten for each test. The tests were performed for (P_i, T_i, E)$\in$[2.55 MPa, 6 MPa]$\times$[-12 °C, 22 °C]$\times$[70 J, 310 J]. The tests are discriminated in three categories :

- Saturation [stars], for the ones performed at, or near, saturation conditions. The saturation curve is plotted in black.

- REP [diamonds with black contours], for the tests performed at thermodynamic similarity with the water circulating in light water reactors.
- Sub-cooled [disks], for the tests performed far from the saturation curve.

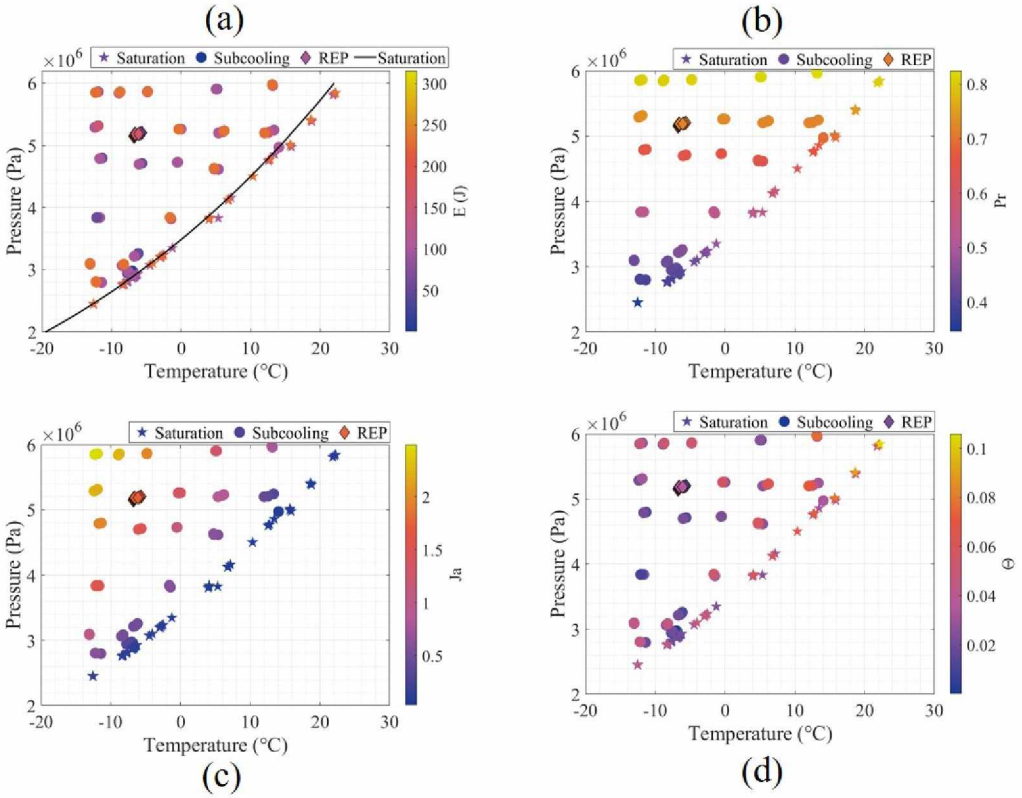

Figure 4: Overview of the thermodynamics conditions for the tests performed in a (P, T) diagram. The colour scale stands for the energy (a), the reduced pressure (b), the Jakob number (c) or the number Θ (d)

To extract tendencies from the tests performed, three dimensionless numbers were used: the reduced pressure, the Jakob number and the number Θ.

The reduced pressure P_r (figure 4b), is the ratio between the static pressure and the critical pressure: $P_r = P_i/P_c$. It ranges between 0.3 (low static pressure) and 0.8 (high static pressure). Several properties involved in the vapour volume growth kinetics, vary according to reduced pressure and in particular the latent heat and the vapour specific volume.

The Jakob number (figure 4c) is the ratio between the sensible heat and the latent heat of the liquid weighted by the ratio of density. Its expression is as follows:

$$Ja = \frac{\rho_l}{\rho_v} \frac{c_{pl}(T_i - T_{sat}(P_i))}{\mathcal{L}} \tag{3}$$

All these properties were extracted from the National Institute of Standards and Technology - NIST (see [15]). For all the tests, the Jakob number ranges between 0.02 (saturation) and 2.25 (high sub-cooling). It outlines the influence of the sub-cooling on the phase change phenomena.

Lastly, the number Θ is the ratio between the mass of vapour, created with an energy E deposited in the liquid, and an arbitrary mass of liquid. It's calculated as follows :

$$\Theta = \frac{E}{c_{pl}(T_i - T_{sat}(P_i)) + \mathcal{L}} \cdot \frac{1}{m_f} \tag{4}$$

Where m_f is the mass of fluid that surrounds the heating element. It's the cross-section area of the test section multiplied by the height of the heating element and multiplied by the density of the liquid. In other words, this number gives the order of magnitude of the quantity of liquid surrounding the heating element that could be vaporized for a given set of initial condition. Then, if $\Theta = 1$, the liquid surrounding the heating element is completely vaporized and if $\Theta = 0$, no vapour is created. For the performed tests, this number Θ is between 0.01 and 0.1 (see figure 4c) and scales the energy deposited within the heating element as a ratio of the surrounding liquid that could be vaporized.

3.2. Influence of the thermodynamic conditions on the maximum of overpressure

The maximum of overpressure, observed at 1.6 ms in figure 2c, is extracted from all the tests performed and plotted on the figure 5. This figure shows the maximum of overpressure for each test in function of the reduced pressure (abscissa) and Θ (colour range).

The figure 5a shows that the maximum of overpressure ranges between 0.3×10^5 Pa (for the highest value of P_r, i.e. $P_r \simeq 0.8$) and 3×10^5 Pa (for the lowest value of P_r, i.e. $P_r \simeq 0.36$). It varies according to both P_r and Θ: it decreases with P_r for a fixed Θ and increases with Θ for a fixed P_r. The rate of decrease in function of P_r increases with an increased of Θ as shown

with fitted curves (second order polynomial fit) plotted with dot lines. For medium to high Θ, i.e. $\Theta \geqslant 0.04$, the overpressure converges to a unique value equal to $0.25{\times}10^5$ Pa for an increasing reduced pressure. However, for low Θ, i.e. $\Theta < 0.02$, the fitted curve doesn't seem to converge to this unique value. This may due to the fact that no test had been performed at $P_r > 0.75$ and $\Theta < 0.02$, the validity of the fit is then limited for low values of Θ.

The decrease of the overpressure with respect to Pr for fixed Θ is interpreted as follows. Constant Θ corresponds to similar kinetics of formation of vapour (same ratio between energy deposited and energy required for mass transfer process) in terms of mass. Nevertheless, as Pr increases, the corresponding volume of vapour generated decreases due to the decrease of vapour specific volume with pressure. Our interpretation relates the overpressure (see section 4) to the internal pressure within the vapour layer during the first stage of its growth: internal pressure has to increase to let the layer volume expand by momentum exchange with surrounding liquid. Therefore, the growth of a smaller vapour volume (e.g. constant Θ and decreasing Pr) leads to lower overpressure.

This tendency is confirmed in figure 5b where the abscissa and the colour scale are inverted from the figure 5a. For low reduced pressure, i.e. $P_r \leqslant 0.5$, the overpressure P_m is increasing with the number Θ: the largest the mass that could be vaporized, the largest the overpressure, showing the influence of the energy deposited in the fluid in regards to the difference of enthalpy. However, for high reduced pressure, i.e. $P_r \geqslant 0.7$, the overpressure exhibits a slow increase until $\Theta = \Theta_1 \simeq 0.025$ and then a very flat variation with regards to Θ at a level that decreases with increasing P_r. Similar reasoning can be considered for explaining the variation of the overpressure with respect to Θ for constant and low values of Pr. For constant Pr, the specific volume of vapour is similar, and increasing theta increases the mass of vapour that is generated by the power input. A larger rate of vapour formation then leads to a larger overpressure during its expansion against surrounding liquid. For the largest Pr values investigated, we observe the overpressure to become less sensitive to Θ variation. This suggests a possible additional limiting process for the vapour layer growth that has not been identified by the authors.

Moreover, there is no clear tendency of variation of P_m with respect to Ja for either P_r or Θ fixed as seen in figure 5c. The overpressure is decreasing with Ja but no other significant tendency could be extracted. Sub-cooling is therefore a second order parameter for the magnitude of the overpressure.

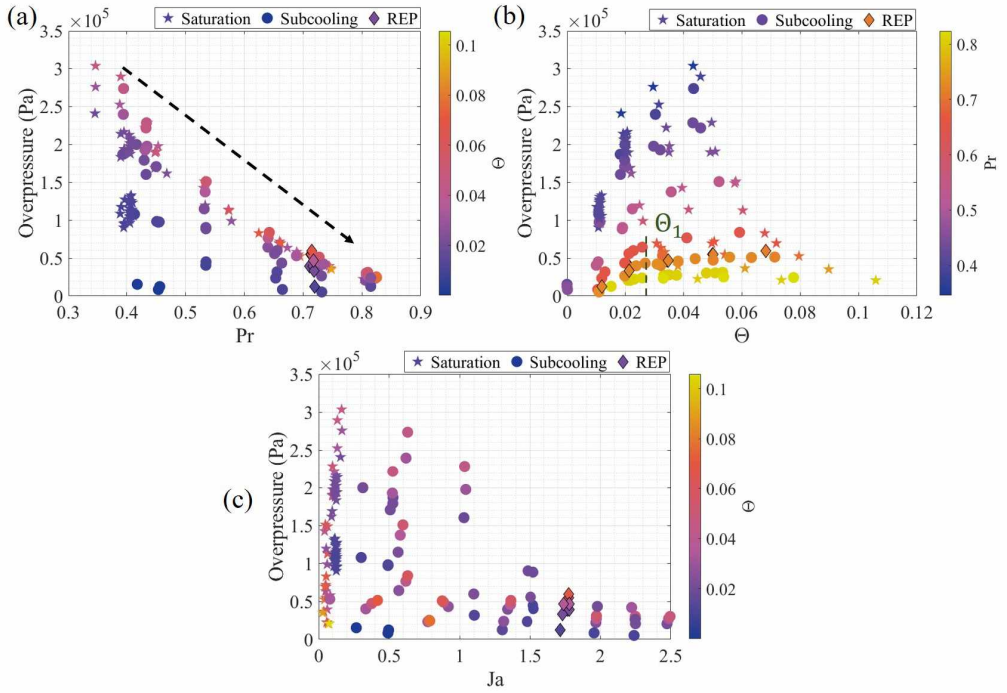

Figure 5: Maximum of overpressure (P_m) function of the reduced pressure, the number Θ and the Jakob number

3.3. Influence of the thermodynamic conditions on the amount of created vapour

The maximal volume of created vapour (V_v) during the test is calculated with equation (1) for each test and plotted on the figure 6. The figure 6a exhibits the created volume (V_v) in function of the hypothetical volume (V_v^{hypo}) presented in figure 3b. The colour scheme represents the influence of the Jakob number on the created vapour. Over the 200 tests performed, V_v ranges from 0.5 to 8 cm^3. V_v is shown to be always less than V_v^{hypo}, that is a logical result since V_v^{hypo} bounds theoretically the amount of vapour that can be generated for the given energy deposited. For zero Jakob values (star symbols), the ratio V_v/V_v^{hypo} is very close to one for low V_v values but decreases with larger V_v values. This ratio clearly decreases with increasing Jakob values. Moreover, an increased Jakob number signifies the increase of subcooling of the fluid and then a quicker recondensation of the vapour in the liquid. The decrease of V_v/V_v^{hypo} with increasing Ja is then interpreted as the impact of liquid subcooling on the recondensation process of the vapour

leaving the plates.

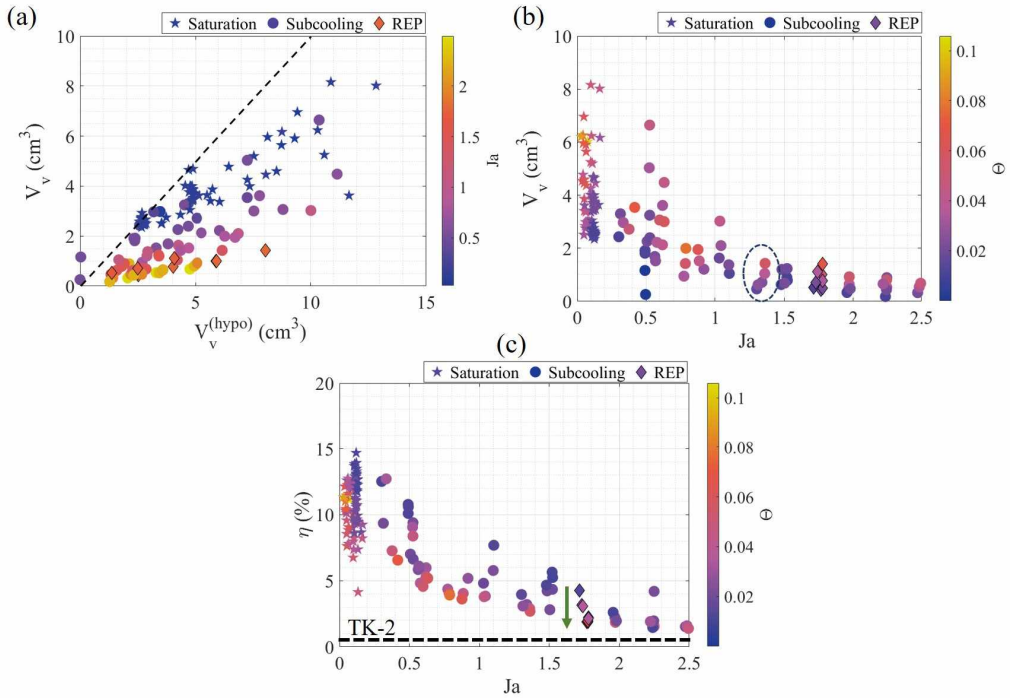

Figure 6: Volume of vapour in function of the theoretical volume created (a) and in function of the Jakob number and Θ (b). (c) η in function of Ja and Θ

The figure 6b shows the calculated volume of vapour (V_v) in function of Ja and Θ (colour map). The volume of vapour is decreasing with the Jakob number due to the increase of the influence of the sensible heat with the Jakob number. Moreover, for a constant Jakob number, $Ja = 1.35$ for example (dot circle), V_v is increasing with Θ because Θ is related to the mass of vapour that could be created with a certain amount of energy.

The ratio between the mechanical energy generated by the creation of vapour and the energy deposited in the fluid is calculated as follows and plotted in figure 6c,

$$\eta = \frac{|P_i V_v|}{\int_0^{+\infty} U(t) I(t) dt} \tag{5}$$

This ratio is interpreted as the efficiency of the creation of vapour and is between 1.4% and 15%. It decreases with Ja showing the influence of the latent heat on the creation of vapour. For a some values of Ja (REP conditions for example), η is decreasing with Θ which shows that for an increasing energy deposited in the tungsten the creation of vapour is less efficient. However, this tendency is not valid for other values of Ja, i.e. saturation tests ($Ja < 0.2$). No clear tendency could then be extracted for the evolution of η with a constant value of Ja.

The observed η are one to two orders of magnitude higher than the η calculated for NSRR tests ($\eta_{(TK-2)} = 0.76\%$ and $\eta_{(JMH-5)} = 0.35\%$), see [16]. However, the NSRR tests were performed for a Jakob number equals to 250 and there is a large uncertainty on the amount of fuel (and therefore energy) involved in the process, since it has been maximized in the evaluation.

4. Theoretical estimation of the first pressure peak

For the tests performed, the maximum of overpressure shows significant tendencies with the reduced pressure and Θ. However, the analysis of these tendencies depends on the test section and is limited by the measurements performed. A simplified model is created to understand the influence of each parameter (pressure, heating surface, etc.).

4.1. Creation of vapour and overpressure

The model is based on the simplified geometry presented on the figure 7. A heated tungsten plane, of wet surface S, is inserted in a liquid at a temperature T_i and a pressure P_i. The difference of temperature between the

tungsten and the liquid generates a layer of vapour which grows over time with a velocity u. This simplified geometric model for the vapour layer at the first instants of vapour generation is mainly supported by our visual observation and deviates from more classical boiling process associated to bubble generation over nucleation sites. The vapour mass at very early stages of its formation is therefore idealized as uniform layer over the plate with a rather smooth interface assumed to be a plane that moves with velocity u. The pressure and the temperature in the volume of vapour are noted $P(t)$ and T_v. The temperature T_v is considered homogeneous in the volume of vapour and equal to the saturation temperature, i.e. $T_v = T_{sat}(P_i)$.

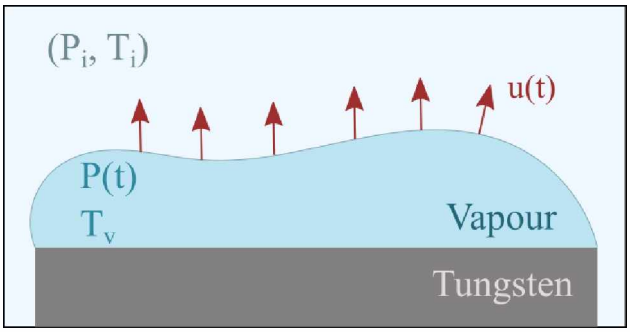

Figure 7: Sketch of the vapour layer growth process

The increase of volume of the vapour is governed by the momentum balance at the liquid side of the interface,

$$\rho_l \frac{\partial u}{\partial t} = -\nabla P \tag{6}$$

The estimation of the pressure gradient is given by the 1D model of wave propagation with a variable pressure at the interface,

$$\nabla P \sim \frac{dP(t)}{dt}\frac{1}{c} \tag{7}$$

Where c is the sound velocity in the liquid. This approximation is valid during the first milliseconds before acoustic wave rebounds interfere in the interfacial pressure evolution. Integration of equation (6) over time then yields to,

$$u(t) = \frac{P(t) - P_i}{\rho_l c} \tag{8}$$

The change of volume of vapour is driven by the velocity of the interface as follows,

$$u(t) = \frac{1}{S}\left(m_v \frac{dv}{dt} + v\frac{dm_v}{dt}\right) \tag{9}$$

With v the specific volume of the vapour and m_v the mass of vapour within the layer. For the carbon dioxide, the specific volume is expressed as,

$$v = \frac{zRT_v}{M_{CO_2}P(t)} \tag{10}$$

The combination of the previous equations gives the following differential equation,

$$\underbrace{\frac{\partial v}{\partial P}m_v(t)}_{<0}\frac{dP}{dt} = \underbrace{-\frac{dm_v}{dt}v(P)}_{<0,(a)} + \underbrace{S\frac{P(t)-P_i}{\rho_l\, c}}_{>0,(b)} \tag{11}$$

The equation (11) shows that the evolution of pressure over time, dP/dt, depends on two mechanisms :

(a) the creation of vapour at a constant volume which tends to increase the pressure;

(b) the expansion of the volume of vapour due to the difference of pressure which tends to decrease the pressure;

The competition between these two mechanisms over time creates the pressure peak due to the transient creation of vapour $m_v(t)$.

4.2. Dimensionless equations and resolution

To obtain a dimensionless differential equation, the following parameters are used,

$$\begin{cases} t^* = t/\tau_{sf} \\ P^* = P/P_i \\ m_v^* = m_v/(\dot{m}_0\tau_{sf}) \end{cases} \tag{12}$$

Where τ_{sf} and $\dot{m}_0$ stand for the time scale of the creation of vapour and the initial mass flow rate of vapour. For the test considered in the following subsection, $\tau_{sf} = 2\,\text{ms}$, $P_i = 2.55\,\text{MPa}$ and $\dot{m}_0 = 0.061\,\text{kg.s}^{-1}$. τ_{sf} and $\dot{m}_0$

have been evaluated from the first instant of the $V_v(t)$ signal. These scales give the following dimensionless equation,

$$\dot{P}^* = -N_1 \frac{1}{m_v^*}(P^*)^2(P^* - 1) + \frac{\dot{m}_v^*}{m_v^*}P^* \tag{13}$$

Where N_1 reads as $N_1 = \frac{\rho_v}{\rho_l}\frac{P_i}{c}S\frac{1}{\dot{m}_0}$. Therefore, N_1 is the parameter that for a given kinetics of vaporization m_v^* determines the pressure peak evolution. Since it scales first term of the right-hand side of equation (13) corresponding to the negative contribution to $\dot{P}^*$, the peak is all the more high than N_1 is small. This link between $\dot{P}^*$ and N_1 qualitatively illustrates how thermodynamic conditions and geometry impact this pressure peak.

From the analysis of all the tests performed and presented on the previous section, the non-dimensional mass of vapour m_v^* is modelled by a first-order system (exponential function),

$$m_v^* = N_0 - e^{-t^*} \tag{14}$$

The differential equation (13) is then fully parametrized by two parameters N_0 and N_1 which expressions are the following,

$$\begin{cases} N_0 = \frac{m_{v,max}}{\dot{m}_0 \tau_{sf}} \\ N_1 = \frac{\rho_v}{\rho_l}\frac{P_i}{c}S\frac{1}{\dot{m}_0} \end{cases} \tag{15}$$

Where $m_{v,max}$ is the maximum of vapour generated (kg).

To conclude, the increase of pressure is completely described by the equation (13), which is a non-dimensional differential equation parametrized by only two dimensionless numbers N_0 and N_1. The resolution of this equation is done by two means presented on the figure 8, which summarizes the process of comparison between experimental data and model results.

The set of equations (E) and (E*) are equations (11) and (13), respectively.

As a first step, an analytical work formally relates the values of (N_0, N_1) to the time t_m^* and the amplitude P_m^* of the pressure peak. The time evolution of pressure is modelled by a polynomial function:

$$P^*(t^*) - 1 \propto (t^*)^2 - 2\frac{t^*}{t_m} \quad (\forall t^* \in [0; t_m^*]) \tag{16}$$

ensuring that $P^*(0) = 1$ and $\left.\frac{dP^*}{dt^*}\right|_{t^*=t_m^*} = 0$.

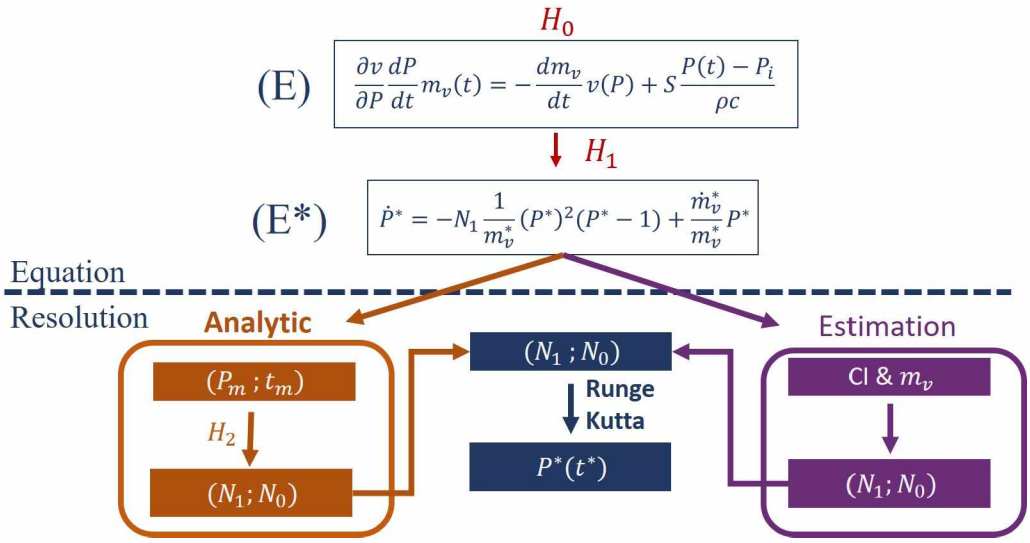

Figure 8: Resolution Diagram

Integration of equation (16) yields the following approximation relation between $(N_0,\ N_1)$ and $(t_m^*,\ P_m^*)$:

$$\begin{cases} N_1 = \frac{e^{-t_m^*}}{P_{t_m}^*(P_{t_m}^*-1)} \\ N_0 = \frac{1}{(1-P_{t_m}^*)}\left[e^{-t_m^*}\left(1+\frac{2t_m^*}{3}\right) - P_{t_m}^*\right] \end{cases} \tag{17}$$

For a given test, one can thus on one hand deduce $(N_0,\ N_1)$ with the equation (15) by using the initial test conditions and estimating the vapour formation kinetics. On the other hand those values can be related to the over-pressure measurement using equation (17). Both approaches are used, the first one being denoted 'Estimated' and the second 'Analytic', to evaluate the adequacy of the model to reproduce our data, as illustrated by the resolution diagram of figure 8. Three major hypotheses are identified: (H_0) for the evaluation of the expansion dynamics reduced to an acoustic model for the pressure gradient, (H_1) for the idealized time evolution of m_v^*, and (H_2) for the idealized quadratic time evolution of P^* for the first peak. (H_1) is based on a macroscopic analysis of the creation and expansion of vapour during the first instants of the deposit of vapour. It is only valid during the first instants of the test (first 5 ms). (H_1) and (H_2) were both extracted from the data analysis (200 tests). The first instants of creation of vapour could be

fitted by a first order exponential function for most of the tests (H_1). The first peak of pressure is well fitted by a second order polynomial function for most of the tests. Furthermore, for a simple model of the first pressure peak, these approximation which use simple function were relevant.

Once the parameters N_0 and N_1 calculated, a Runge-Kutta algorithm is used to solve the equation (13) and to calculate the non-dimensional overpressure over non-dimensional time, i.e. $P^*(t^*)$. The results of these calculations are presented on the figure 9.

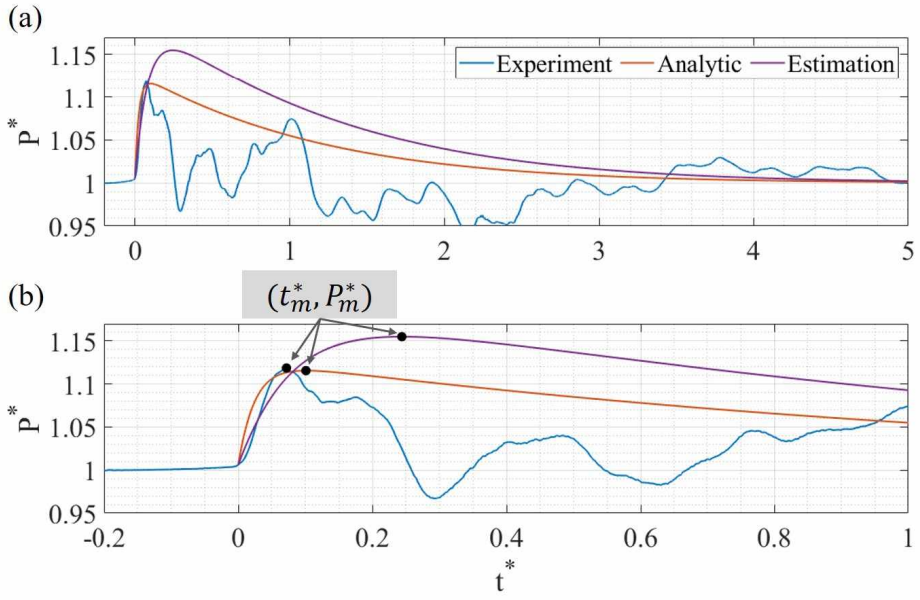

Figure 9: Pressure calculation (*Analytic* and *Estimation*) compared to the experimental result (*Experiment*). The sub-figure (a) is the raw result and the sub-figure (b) is a zoomed frame of the results.

This figure is divided in two subfigures and presents the non-dimensional overpressure over a non-dimensional time range of $t^* \in [-0.2; 5]$ (figure 9a) and $t^* \in [-0.2; 1]$ (figure 9b). The original time scale presented on the figure 5 has been changed to use the start of the overpressure increase as the origin. The measured pressure (**Experiment**) exhibits a first peak which reaches a maximum of 1.1186 at $t_m^* = 0.072$ before decreasing toward zero. The calculated overpressures (**Analytic** and **Estimation**) sharply increase toward a maximum before slowly decreasing to zero. The increase of pressure exhibits the same trend as the experiment. However, the decrease of the overpressure

is an envelope curve of the experimental overpressure. This envelope does not show the same oscillating behaviour because the acoustic rebounds in the test section are not taken into account in the model. Acoustic rebounds that are associated to the interpretation of pressure oscillations after the first peak cannot be recovered by the model since equation (7) is strictly valid for an infinite liquid domain surrounding the vapour layer: as soon as acoustic waves interfere with pressure near the interface, pressure gradient governing the model for the vapour layer overpressure deviates from the observations. It is first underestimated by the model that leads to a smoother decrease of the overpressure with respect to the recorded signal. Further time evolution of pressure wave leads to several oscillations that cannot be represented as well. To this extend, the model can only provide an envelope estimation of the overpressure decrease.

All three curves exhibit the same trend but does not share the same maximum. This is clearer in figure 9b on which the maxima are highlighted with black dots (t_m^*, P_m^*). The results of both computations are summarized in the table 1 where the calculation error is expressed as a percentage as: $\epsilon_P = \left(P^*_{t_m,calc} - P^*_{t_m,exp}\right)/P^*_{t_m,exp}$ and $\epsilon_t = \left(t^*_{m,calc} - t^*_{m,exp}\right)/t^*_{m,exp}$. In these equations, *calc* stands for 'calculation' (Analytic or Estimation) and *exp* for 'experiment'.

	P_m^*	ϵ_P (%)	t_m^*	ϵ_t (%)
Experiment	1.1186	×	0.072	×
Analytic	1.1156	-0.27	0.101	40
Estimation	1.155	3.3	0.24	233

Table 1: Value of the maximum of overpressure calculated (**Analytic** and **Estimation**), and its instant of occurrence, compared with the experiment's one (**Experiment**)

The calculated maxima of non-dimensional overpressure are of the same order of magnitude as the experimental value, i.e. the error ϵ_P is under 5%. However, the estimated value ($P_m^* = 1.155$) is higher than the experimental one by a factor 1.03. This is due to the estimated mass of vapour that relies on an exponential assumption, which is just an approximation of how the mass of vapour is created and could then imply an error.

The gap between the experiment and the calculation are higher for the instant of the maximum of pressure (t_m^*). It is of the same order of magnitude

for the analytic (around 0.1), but it shows a major difference for the estimation. The calculated error is higher than 10%, for both cases, which translates a major uncertainty on the calculation of the instant of the maximum of pressure. This difficulty could be put in perspective of the non-dimensional time scale which is small: between 0 and 0.4 which is equivalent to $t \in [0;\ 0.8]$ ms.

In conclusion, the resolution of the equation (13) gives two plots: the analytic calculation and the estimation one. Both curves show the same trend and are envelope curves of the experimental pressure. This shows that the model can reproduce the overpressure dynamics. But the curves exhibit higher overpressure maximum which occurs later on non-dimensional scale. From the observed differences, an uncertainty of calculation is extracted. However, it is considered small concerning the pressure and time scale which validate the calculation performed.

4.3. Parametric influence on the overpressure

For the test studied in the previous subsection, the parameter N_0 does not vary significantly between both calculations which translate a well-described creation of vapour. However, the change of N_1 implies great changes in the overpressure plot. To understand the significance of N_1 variation, we consider that we model tests with similar vapour mass generation dynamics on a similar heating element. Therefore N_1 variations are related to thermodynamics conditions variation through variation of $(\rho_v/\rho_l)(P_i/c)$. Analysis of the variations of thermodynamic properties over the range of our experimental data shows that $(\rho_v/\rho_l)(P_i/c)$ is mainly an increasing function of P_i. Therefore, variation of the overpressure predicted by the model for fixed N_0 and increasing N_1 has to be related to the variation with respect to the initial pressure, say the parameter P_r.

The resolution is performed for $N_1 \in [1, 10]$ and the non-dimensional overpressures calculated are plotted on the figure 10 on a non-dimensional time scale between 0 and 2. The change of N_1 is shown with a different colour from one test to another.

The non-dimensional overpressures calculated are between 1 and 1.4 and exhibit the same kinetic as the one observed on the figure 9: a quick increase to a maximum value and a slow decrease to zero. The increasing value of N_1, i.e. increasing brightness of the curve, exhibits a decrease of the maximum overpressure and a smaller t_m^*. The decrease of the maximum of overpressure with the static pressure is equivalent to the tendency observed on the figure 9.

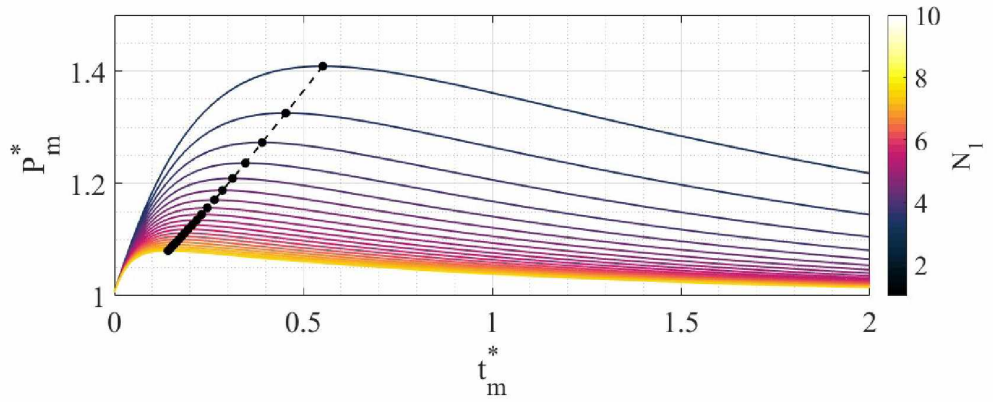

Figure 10: Overpressure calculated for different N_1 and by considering the same vapour generation and the same heated surface

The values of P_m^* and Γ_m in function of N_1 are presented on the figure 11. The non-dimensional overpressure (11-a) is decreasing with N_1 and its values range between 1 and 1.4. The decrease of P_m^* in function of N_1 could be fitted with a power function of the form $f(N_1) = a \times N_1^b + c$. It is plotted in figure 11a with $(a,\ b,\ c)$=(0.47, -0.52, 0.94).

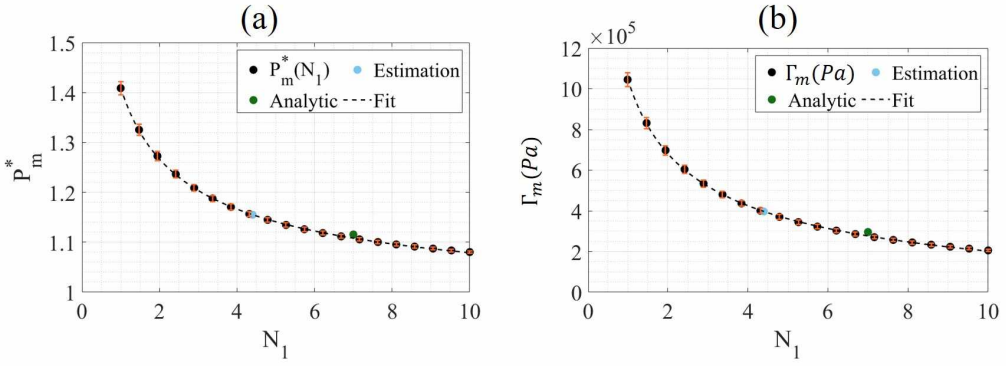

Figure 11: Maximum of overpressure (non dimensionnal) extracted from the calculation presented on the figure 10 with the corresponding uncertainties (a), and the corresponding maximum of overpressure in Pascal (b). Both curves are fitted with a power function

The dimensional overpressure (Γ_m) in function of N_1 is plotted in figure 11b. It shows the same trend: a decrease of Γ_m in function of N_1 which could be fitted with a power curve. In this case, $(a, b, c) = (1.21 \times$

$10^6, -0.52, -1.63 \times 10^5$). The calculated overpressure is between $2{\times}10^5$ Pa and $10.5{\times}10^5$ Pa which is of the same order of magnitude as the ones observed experimentally (see figure 5). Therefore the model predicts a similar trend with similar order of magnitude for the evolution of the overpressure amplitude with respect to the initial pressure level.

However, this study of the influence of N_1 on the maximum of overpressure is limited without a clearer link between the non dimensionnal test numbers, i.e. (Ja, P_r, Θ), and the non dimensionnal modelling numbers, i.e. (N_0, N_1). This work of identification from a group of numbers with another is a perspective of the present work.

5. Conclusion

The presented experiment permits to study the influence of the thermodynamics conditions on thermal shock phenomena. To characterize the phenomena, a first test is studied for (P_i, T_i, E)=(2.55 MPa, -12.5 °C, 232 J). From the powerful discharge of 9 capacitors, the quick heat up of tungsten sheets ($dT/dt = 19 \times 10^3$ K.s^{-1}) produces a fine layer of vapour which generates a pressure wave of $3{\times}10^5$ Pa in less than 1 ms. The maximum of volume of vapour is obtained at 0.3 s after the power deposit and is equal to 9 cm^3. In order to characterize the phenomena, two quantities are extracted: the maximum of overpressure produced by the quick creation of vapour and the maximum of vapour generated.

To study the influence of the thermodynamic conditions on the phenomena, 200 tests were performed for (P_i, T_i, E)$\in$[2.55 MPa, 6 MPa]$\times$[-12 °C, 22 °C]$\times$[70 J, 310 J]. Three main parameters are extracted from these tests conditions (P_r, Ja and Θ), and used to seek tendencies of the maximal overpressure and the volume of created vapour. The maximum of overpressure shows a noticeable decrease with reduced pressure and mixed tendencies with Θ. The volume of vapour shows a clear decrease with the Jakob number which represents the influence of the subcooling of the fluid on the phenomena.

The performed tests permit extracting tendencies of the maximum overpressure but the thermodynamics ranges are limited. To predict the phenomena further on the thermodynamic scales, a theoretical model has been built. It relies on the mass and momentum balance equation of the creation of vapour during the first instants, summed up in a first order differential equation. From this equation a dimensional analysis is performed to obtain a

non dimensional equation which is parametrized by two quantities: N_0 that parametrizes the dynamics of vapour formation and N_1 that combines the scales of the pressure variation process. The model is then validated using the experiment analysed in the first section of this paper. The parametric study performed shows that the model consistently predicts the variation of the overpressure peak with respect to the static pressure level observed in the experiments.

The model built shows some interesting results but is still limited in the interpretation of the experimental results. More particularly, the link between the couple (N_0, N_1) and the experimental triplet (Ja, P_r, Θ) should be clarified for allowing a more predictive use of the model. Concerning the experiment performed, they show interesting tendencies but are still limited due to the heating element which vibrates for $E > 300$ J. The current work concerns the improving of the heating element to perform tests at higher energy levels.

6. Acknowledgements

This work is funded by Électricité de France (EDF) and Institut de Radioprotection et de Sûreté Nucléaire in the frame of their collaborative research programs. The authors would thank the technical staff and the engineers who permit the mounting of the experimental test section in INSA Lyon, CETHIL.

Appendix A. Study of the uncertainties

The uncertainties on the measured quantities presented in this paper are calculated as a quadratic composition of type A and type B uncertainties, see [17]. The type B uncertainties are the so-called measurement chain uncertainties and are calculated by the combination of all uncertainties in the measuring chain. These calculations are presented in [11].The type A uncertainties are statistically calculated thanks to repeatability tests done before and after the main test campaign (the 200 tests presented in this paper) which are composed of 9 and 12 tests, respectively, of experiments realized with the same test conditions (same thermodynamic conditions and energy deposited). The results obtained before and after the main campaign do not show significant disparities from one to another which show a strong consistency between all the experiments performed in this paper.

The expanded composed uncertainty of a variable X, U_X^c is then calculated as follows,

$$U_X^c = \sqrt{\left(k^{(A)} u_c^{(A)}\right)^2 + \left(k^{(B)} u_c^{(B)}\right)^2} \tag{A.1}$$

With k and u_c the coverage factor (equals to 2 for the type B and equals to the Student's number for the type A) and the combined uncertainty of the variable, respectively. For each value presented in this paper, U_X^c is calculated and presented in the table A.2,

Variable	**Type de variable**	U_X^{mes}	U_X^{rep}	U_X^c	U_X^c/X **(%)**
P_i (bar)	Static pressure	1.16	0.15	1.17	3.9
T_i (K)	Temperature	0.99	0.2	1.01	0.38
E(J)	Energy	0.0033	0.67	0.67	1.22
Γ(Pa)	Overpressure	555	5.52×10^3	5.6×10^3	5
V_v(cm^3)	Volume of vapour created	-	0.15	0.15	5.4

Table A.2: Uncertainties of the variable measured and calculated in the experiment

For the figure presented in this paper, the uncertainty bars were not plotted to facilitate the read. The dots and points used are of the same size as these bars, as shown on the following figure (figure A.12). On this figure is plotted the thermodynamics conditions (a), the overpressure function of the reduced pressure (b) and the volume of vapour function of the Jakob number (c), for all the tests. These subfigures are respectively the subfigures 4a, 5a and 6b.

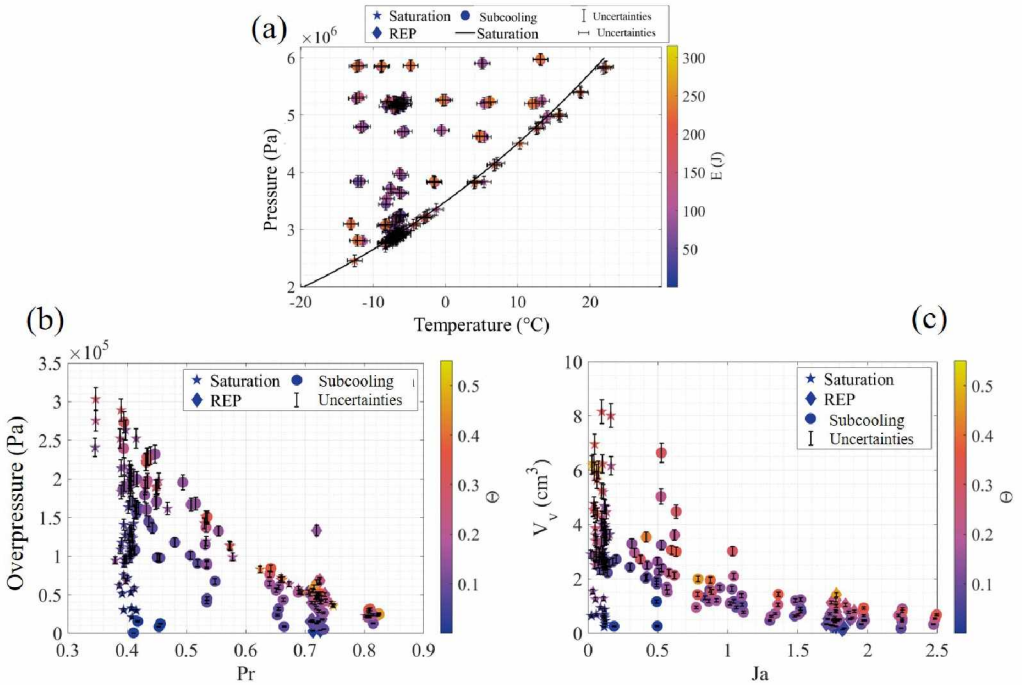

Figure A.12: Uncertainties plotted with bars for the quantities of interest: thermodynamic conditions (a), Γ_m (b) and V_v (c)

References

[1] D. D. Imholte, F. Aydogan, Comparison of nuclear pulse reactor facilities with reactivity-initiated-accident testing capability, Progress in Nuclear Energy 91 (2016) 310–324. doi:10.1016/j.pnucene.2016.05.012.

[2] M. Ishikawa, S. Shiozawa, A study of fuel behavior under reactivity initiated accident conditions — review, Journal of Nuclear Materials 95 (1–2) (1980) 1–30, number: 1–2. doi:10.1016/0022-3115(80)90076-8.

[3] C. Bernaudat, J. Delplace, P. Lafon, L. Antoinat, Consequences of leaking fuel rod failure during RIA transients - paper A0208, in: TopFuel 2018, Praha, Czech Republic, 30 sept. - 04 oct., 2018, pp. 1–10.

[4] C. Bernaudat, H. Billat, J. Vermoyal, N. Waeckel, A. Kececioglu, Updated RIA criteria in France - paper A0209, in: TopFuel 2018, Praha, Czech Republic, 30 sept. - 04 oct., 2018, pp. 1–9.

[5] B. Biard, V. Chevalier, C. Gaillard, V. Georgenthum, Q. Grando, J. Guillot, L. Lebreton, C. Manenc, S. Mirotta, N. Monchalin, Reactivity Initiated Accident transient testing on irradiated fuel rods in PWR conditions: The CABRI International Program, Annals of Nuclear Energy 141 (2020) 107253. doi:https://doi.org/10.1016/j.anucene.2019.107253.

[6] T. Sugiyama, T. Fuketa, Mechanical Energy Generation during High Burnup Fuel Failure under Reactivity Initiated Accident Conditions, Journal of Nuclear Science and Technology 37 (10) (2000) 877–886. doi:10.1080/18811248.2000.9714968.

[7] Z. Zhao, S. Glod, D. Poulikakos, Pressure and power generation during explosive vaporization on a thin-®lm microheater, Int. J. Heat Mass Transfer (2000) 16.

[8] S. Glod, D. Poulikakos, Z. Zhao, G. Yadigaroglu, An investigation of microscale explosive vaporization of water on an ultrathin Pt wire, International Journal of Heat and Mass Transfer 45 (2) (2002) 367–379. doi:10.1016/S0017-9310(01)00158-2.

[9] A. Abbate, Etude expérimentale d'une interaction thermique au sein d'un fluide, Ph.D. thesis, Université de Lyon, INSA Lyon (2018).

[10] J. Muller, R. Rulliere, A. Abbate, P. Ruyer, M. Clausse, First characterization of two phase phenomena occurring during a rapid energy discharge in saturated carbon dioxide, Experimental Thermal and Fluid Science 129 (2021) 110471. doi:10.1016/j.expthermflusci.2021.110471.

[11] J. Muller, Contribution à l'étude expérimentale d'un choc thermique au sein du dioxyde de carbone, Ph.D. thesis, Université de Lyon, INSA Lyon (Oct. 2021).

[12] A. Sakurai, Mechanisms of transitions to film boiling at CHFs in subcooled and pressurized liquids due to steady and increasing heat inputs, Nuclear Engineering and Design 197 (3) (2000) 301–356. doi:10.1016/S0029-5493(99)00314-3.

[13] Y. Iida, K. Okuyama, K. Sakurai, Boiling nucleation on a very small film heater subjected to extremely rapid heating, International Journal of Heat and Mass Transfer 37 (17) (1994) 2771–2780. doi:10.1016/0017-9310(94)90394-8.

[14] V. P. Carey, Liquid-Vapor Phase-Change Phenomena : An Introduction to the Thermophysics of Vaporization and Condensation Processes in Heat Transfer Equipment, 3rd Edition, CRC Press, 2020. doi:10.1201/9780429082221.

[15] E. W. Lemmon, M. O. McLinden, D. G. Friend, National Institute of Standards and Technology (U.S.), Thermophysical properties of fluid systems, NIST, 1998, oCLC: 84549093.

[16] T. Sugiyama, M. Umeda, T. Fuketa, H. Sasajima, Y. Udagawa, F. Nagase, Failure of high burnup fuels under reactivity-initiated accident conditions, Annals of Nuclear Energy 36 (3) (2009) 380–385. doi:10.1016/j.anucene.2008.12.003.

[17] BIPM, Guide to the expression of uncertainty in measurement, International Organization for Standardization, 2008.